

Supplementary Information

Highly Catalytically Active CeO_{2-x}-Based Heterojunction Nanostructures with Mixed Micro/Meso-Porous Architectures

Sajjad S. Mofarah^{a,*}, Luisa Schreck^a, Claudio Cazorla^b, Xiaoran Zheng^a, Esmaeil Adabifiroozjaei^{c,d}, Constantine Tsounis^e, Jason Scott^e, Reza Shahmiri^a, Yin Yao^f, Roozbeh Abbasi, Yuan Wang^{h,i}, Hamidreza Arandiyani^{ij}, Leigh Sheppard^k, Vienna Wong^a, Esmail Doustkhah^l, Pramod Koshy^a, and Charles C. Sorrell^{a*}

* Sajjad S. Mofarah E-Mail: s.seifimofarah@unsw.edu.au
Charles C. Sorrell E-Mail: c.sorrell@unsw.edu.au

- a. School of Materials Science and Engineering, UNSW Sydney, Sydney, NSW 2052, Australia
- b. Departament de Física, Universitat Politècnica de Catalunya, Campus Nord B4-B5, E-08034 Barcelona, Spain
- c. Research Center for Functional Materials (RCFM), National Institute for Materials Science (NIMS), Tsukuba, Ibaraki 305-0047, Japan
- d. Advanced Electron Microscopy Division, Institute of Materials Science, Technische Universität Darmstadt, Alarich-Weiss-Strasse 2, 64287 Darmstadt, Germany
- e. Particles and Catalysis Research Group, School of Chemical Engineering, UNSW Sydney, Sydney, NSW 2052, Australia.
- f. Electron Microscopy Unit (EMU), Mark Wainwright Analytical Centre, UNSW Sydney, Sydney, NSW 2052, Australia
- g. School of Chemical Engineering, UNSW Sydney, NSW 2052, Australia
- h. School of Chemistry, UNSW Sydney, Sydney, NSW 2052, Australia
- i. Centre for Advanced Materials & Industrial Chemistry (CAMIC), School of Science, RMIT University, 124 La Trobe Street, Melbourne VIC 3000, Australia
- j. Laboratory of Advanced Catalysis for Sustainability, School of Chemistry, University of Sydney, NSW 2006, Australia
- k. School of Engineering, Western Sydney University, Penrith, NSW, 2751, Australia;
- l. International Center for Materials Nanoarchitectonics (MANA), National Institute for Materials Science (NIMS), 1-1 Namiki, Tsukuba, Ibaraki 305-0044, Japan

Experimental

Reagents and materials

Ce(NO₃)₆·6H₂O (99.0%), Mn(NO₃)₂·4H₂O, Cu(NO₃)₂·3H₂O, and triethanolamine (≥98.0%) were purchased from Sigma Aldrich. The trichloroacetic acid (Cl₃CCOOH) (≥99.0%) was purchased from Chem-supply Pty Ltd. For electrochemical setup, a platinum plate (A = 4 cm²), and Ag/AgCl (Basi Inc., Evansville, IN, USA) were used as the counter and reference electrodes, respectively. A Fluorine-doped tin oxide on glass (FTO; Wuhan Geao Scientific Education Instrument, Wuhan, China; film resistivity ~21 Ω sq⁻¹) was also used the working electrode.

Characterisation

Electron microscopy (EM)

The powders were suspended in deionised water and drop-casted on a carbon-coated Cu grid, followed by drying at room temperature. The prepared samples were used for transmission electron microscopy (TEM), high-resolution transmission TEM (HRTEM) images and selected area electron diffraction (SAED) patterns using a Philips CM 200 TEM (Eindhoven, the Netherlands); the EELS analyses were done using a JEOL JEM-ARM200F TEM (Tokyo, Japan). Scanning electron microscopy (SEM) imaging and energy dispersive X-ray (EDS) analyses were obtained using an FEI Nova NanoSEM (Hillsboro, OR, USA) in first and secondary emission modes with accelerating voltage between 10-15 kV.

X-ray photoelectron spectroscopy (XPS)

Surface analysis of the samples was conducted using a Thermo Fisher Scientific ESCALAB 250Xi spectrometer (Loughborough, Leicestershire, UK) equipped with a monochromatic Al K_α source (1486.6 eV) hemispherical analyser. The chamber pressure during the analysis was kept constant at <8-10 mbar. The acquired binding energies were referenced to the C1s signal corrected to 285 eV and the spectra were fitted using a convolution of Lorentzian and Gaussian profiles.

X-ray diffraction (XRD)

Mineralogical data for the nanostructures were obtained using a Philips X'Pert Multipurpose X-ray diffractometer (Almelo, Netherlands) with CuK_α radiation, 40 kV, 20 mA, scan range 20°-70° 2θ, and scan speed 0.2 2θ/min. The peaks were analysed using X'Pert High Score Plus software (Malvern, UK).

Laser Raman microspectroscopy (Raman)

Raman data were obtained by a Renishaw inVia confocal Raman microscope (Gloucestershire, UK) equipped with a helium-neon green laser (514 nm) and diffraction grating of 1800 grooves/mm. All Raman data were recorded over the range 200-1500 cm⁻¹ (with resolution 1 cm⁻¹), laser power 35 mW, and spot size ~2 μm. The spectra were calibrated against the silicon peak at ~ 520 cm⁻¹.

Specific surface area (SSA)

Specific surface areas and pore size distributions of the samples were obtained using the N₂ physisorption technique at -196°C on a Micrometric Tristar 3030. The SSAs and pore size distributions were determined using the Brunauer-Emmett-Teller (BET) and Barrett-Joyner-Halenda (BJH) methods, respectively. Prior to analysis, the samples were degassed under vacuum at 150 °C for 3 h on a Micromeritics Smart VacPrep unit.

Electron paramagnetic resonance (EPR)

EPR analysis for all the samples was conducted using a Bruker EMX X-Band ESR Spectrometer with constant frequency at 9.8 GHz. The EPR data were recorded over the centre field at 3200 mT, modulation amplitude at 4 G, and microwave power at 0.6325 mW. The processing on EPR spectra were carried out using Bruker Xenon software. In order to highlight the presence of oxygen vacancies and defects in the ceria structure, both Ce-CP and 2D-3D CeO_{2-x} were heat treated in N₂ atmosphere and kept in desiccator until the characterisation is done.

Atomic force microscopy (AFM)

The thickness of the nanosheets was measured using AFM (Bruker Dimension Icon SPM, PeakForce Tapping mode). The samples were printed on glass substrates from the top of a homogenous nanosheet/DI water suspension and then fixed onto the AFM stage using a slight vacuum. A ScanAsyst-Air probe (Bruker Nano Inc.) was installed in the AFM holder and used for all measurements. The pixel resolution was 512 samples/line. The scan size was set to 2 by 2 μm , with a scan rate of 0.7 Hz. The peak force set point and the feedback gain settings were optimized accordingly. The AFM images were processed using Nanoscope Analysis 1.7 and the thickness of the holey 2D nanosheets was determined using the height profile from the processed images.

Density functional theory simulations

First-principles calculations based on density functional theory (DFT)¹ were performed to further characterise the oxidation of CO molecules on the surface of 2D CeO_{2-x} heterojunction nanostructures at the atomic level. The PBEsol functional² as implemented in the VASP software was used.³ A “Hubbard- U ” scheme⁴ with $U = 3$ eV was employed for better treatment of the localized Ce $4f$ electronic orbitals. The “projector augmented wave” method was used to represent the ionic cores⁵ by considering the following electrons as valence: Ce $4f$, $5d$, $6s$, and $4d$; Cu $3d$ and $4s$; Mn $3d$ and $4s$; and O $2s$ and $2p$. Wave functions were represented in a plane-wave basis truncated at 650 eV. For integrations within the Brillouin zone Monkhorst-Pack k -point grids with a density equivalent to that of $16 \times 16 \times 16$ in the fluorite CeO_2 unit cell were employed. Geometry relaxations were performed with a conjugate-gradient algorithm that allowed for volume and shape variations of the simulation cell. The relaxations were halted when the forces in the atoms were all below $0.01 \text{ eV} \cdot \text{\AA}^{-1}$. By using these technical parameters, zero-temperature energies that were converged to within 0.5 meV per formula unit were obtained.

Two-dimensional ceria nanosheets were simulated as two-unit cells thick CeO_2 slabs oriented along the $\{111\}$ direction (with chemical formula $\text{Ce}_{16}\text{O}_{32}$). A vacuum region of 25 \AA was considered in all the simulations and periodic boundary conditions were applied along with the three Cartesian directions. Determination of the energetically most favourable Mn and Cu adsorption sites was performed by analyzing all possible positions on the surface of the nanosheet. For all the considered species, the preferred transition metal adsorption site was found to be on top of the circumcentre of the triangle formed by three neighbouring oxygen atoms in the surface of the nanosheet. The content of transition metal ions in the DFT simulations was 6% in reference to the number of cerium atoms. An oxygen vacancy was subsequently created on the surface of the equilibrium MnO and CuO-decorated ceria systems, as close as possible to the transition metal site but without affecting its adsorption mode. The climbing image nudged elastic band (CI-NEB) approach was used to simulate the oxidation of the CO molecule on the surface of the generated 2D CeO_{2-x} heterojunction nanostructures.^{6,7} The reaction energy for each reaction step was calculated as the difference between the corresponding equilibrium final and initial states, whereas the activation energy barrier was calculated as the energy difference between the corresponding transition state and the equilibrium initial state. The convergence of the reaction path relaxation was confirmed by a threshold value on the atomic forces of $0.05 \text{ eV} \cdot \text{\AA}^{-1}$.

Methods

Synthesis of Ce-CP rod precursors

The synthesis was conducted by a chronopotentiometry technique using an electrochemical station (Ezstat Pro, Crown Point, IN, USA, with a resolution of 300 μV and 3 nA in the $\pm 100 \mu\text{A}$ range) with a conventional three-electrode configuration system. The initial electrolytes were prepared by adding 0.05 M TCA and 0.05 M $\text{Ce}(\text{NO}_3)_3 \cdot 6\text{H}_2\text{O}$ in a DI water to make 150 ml of mixed aqueous solution. The pH value was initially found to be 4.2 and was subsequently adjusted to 6.2 using concentrated 3M NaOH solution. Prior to the synthesis of Ce-CP, the FTO substrates were sterilised by ultrasonication in ethanol and acetone (5 min for each). This was followed by immersion (1 cm) in 40% nitric acid for 2 min to activate the surface. The applied constant currents were varied from 3 mA to 30 mA, subject to the surface area of the working electrode (FTO), which was in the range of 1.5 to 15 cm^2 .

Synthesis of Ce-CP and derived CeO_{2-x} morphologies

To synthesise the bulk CeO_2 nanotubes, the Ce-CP precursor was dispersed in strong basic 1M NaOH aqueous solution and rested for 30 min following by centrifuging at 5000 rpm for 10 min. The resultant Ce-NTs were dried at 80°C for 24 h and heat treated to 200 for 3 h. The 2D-3D CeO_{2-x} nanostructure was fabricated by dispersing the Ce-CP tubes (300 mg) in 4ml of pure TEA solution at room temperature for 10 min using a magnetic stirrer at 100 rpm. The liquid was then transferred to a furnace and calcined at 450°C using

different heating rates, as shown in Fig. S2, with dwelling time of 3h. The resulting samples were collected and kept in a sealed container for the ensuing characterisation and application tests. The TMO-based hybrid nanostructures were synthesised using the same approach as the CeO_{2-x} , except the 2 mol% of the TM salts, which are $\text{Mn}(\text{NO}_3)_2 \cdot 4\text{H}_2\text{O}$ and $\text{Cu}(\text{NO}_3)_2 \cdot 3\text{H}_2\text{O}$, were added to the dispersion containing the Ce-CP.

Air purification

The CO oxidation catalytic activity was evaluated using a fixed-bed quartz tubular microreactor (ID = 6.0 mm) at atmospheric pressure. 30 mg of catalyst was used without pre-treatment. The reaction gas (10 sccm CO + 15 sccm O_2 + 80 sccm N_2) with a total flow rate of 105 mL/min was introduced to the reactor, giving a gas hourly space velocity of $\sim 210,000 \text{ mL} \cdot (\text{g h})^{-1}$. The concentrations of the reactants and products in the reactor effluent at incremental reaction temperature steps were monitored on-line by a gas chromatograph (GS; Young Lin 6500, Gyeonggi-do, Republic of Korea) equipped with a thermal conductivity detector (TCD) and a Carboxen-1010 PLOT column. The long-term stability of the CeO_2 catalyst was assessed over a period of 10 h at a constant temperature of 165°C. It was found that the CO conversion at this temperature was maintained at approximately 100%, indicating that the catalyst was stable over this period. The reusability of the catalyst was also assessed by repeatedly cycling the temperature up to 170°C, or until 100% CO conversion was reached. The catalyst performance remained relatively consistent between each cycle, with a slight decrease in performance observed between the 1st and 4th cycle (T_{50} of the first cycle was 150°C, while T_{50} of the fourth cycle was 155°C).

Additional Characterisation

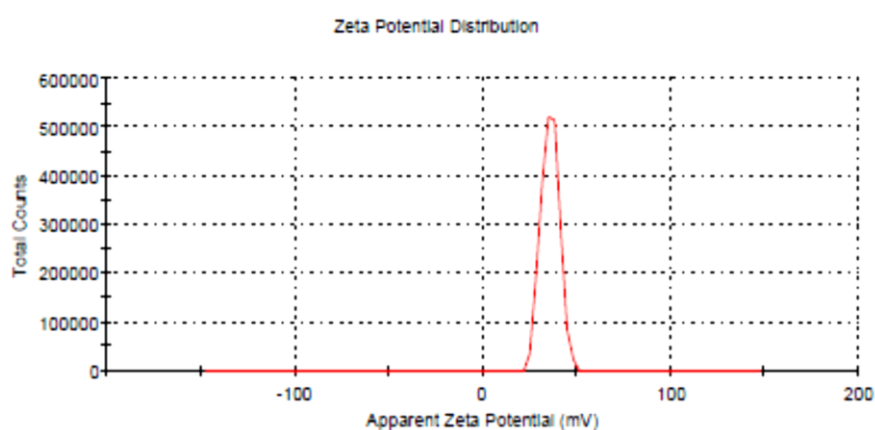


Figure S1: Zeta potential results for Ce-CP dispersed in TEA

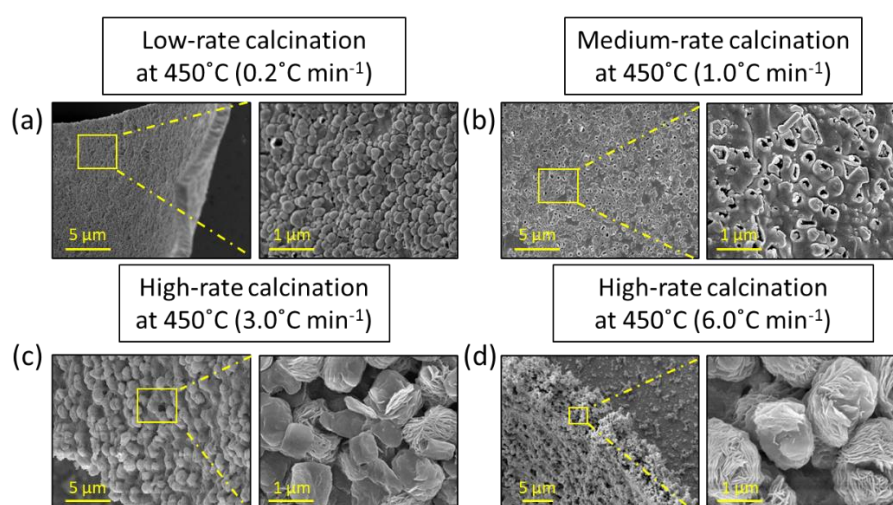


Figure S2: SEM images of CeO_{2-x} obtained at 450°C at different heating rates: (a) low-rate calcination at $0.2^\circ\text{C min}^{-1}$, (b) medium-rate calcination at $1.0^\circ\text{C min}^{-1}$, (c) high-rate calcination at $3.0^\circ\text{C min}^{-1}$, (d) high-rate calcination at $6.0^\circ\text{C min}^{-1}$.

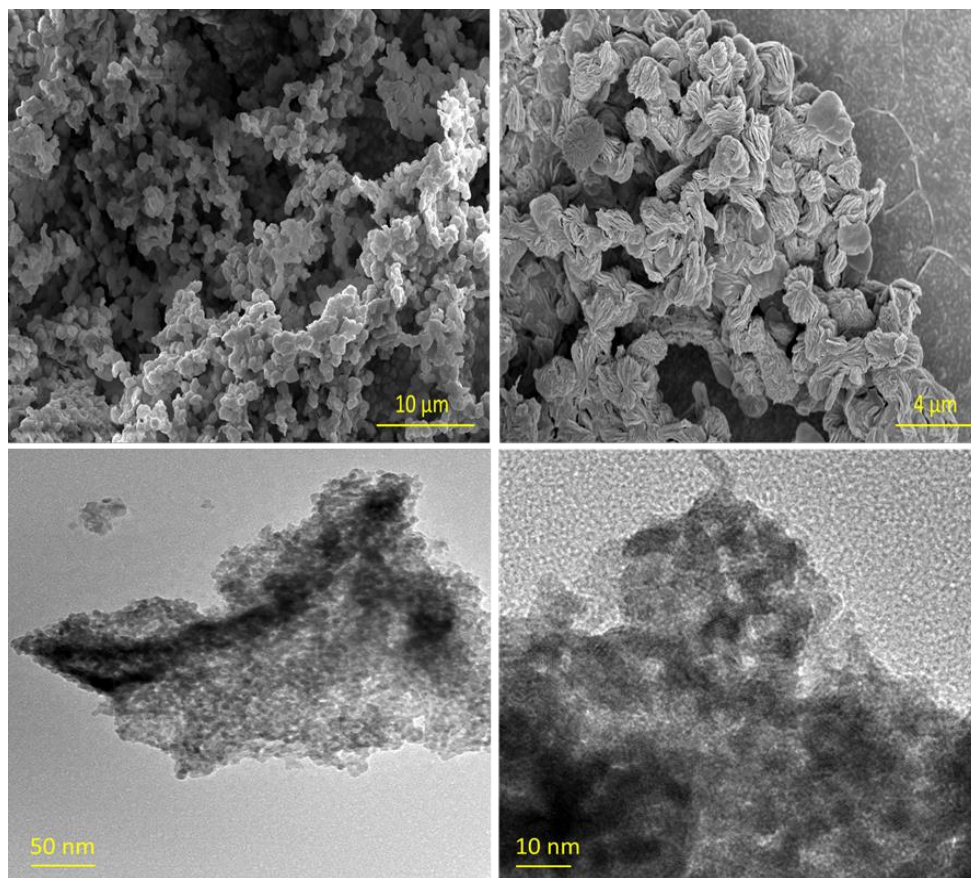


Figure S3: SEM and TEM images of Mo-Ce obtained by rapid calcination

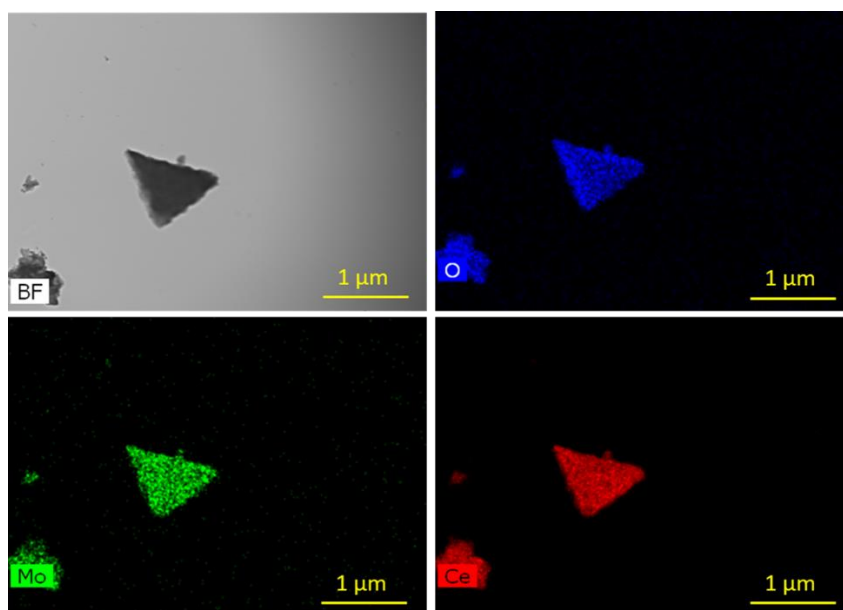


Figure S4: EDS mapping of Mo-Ce obtained by rapid calcination

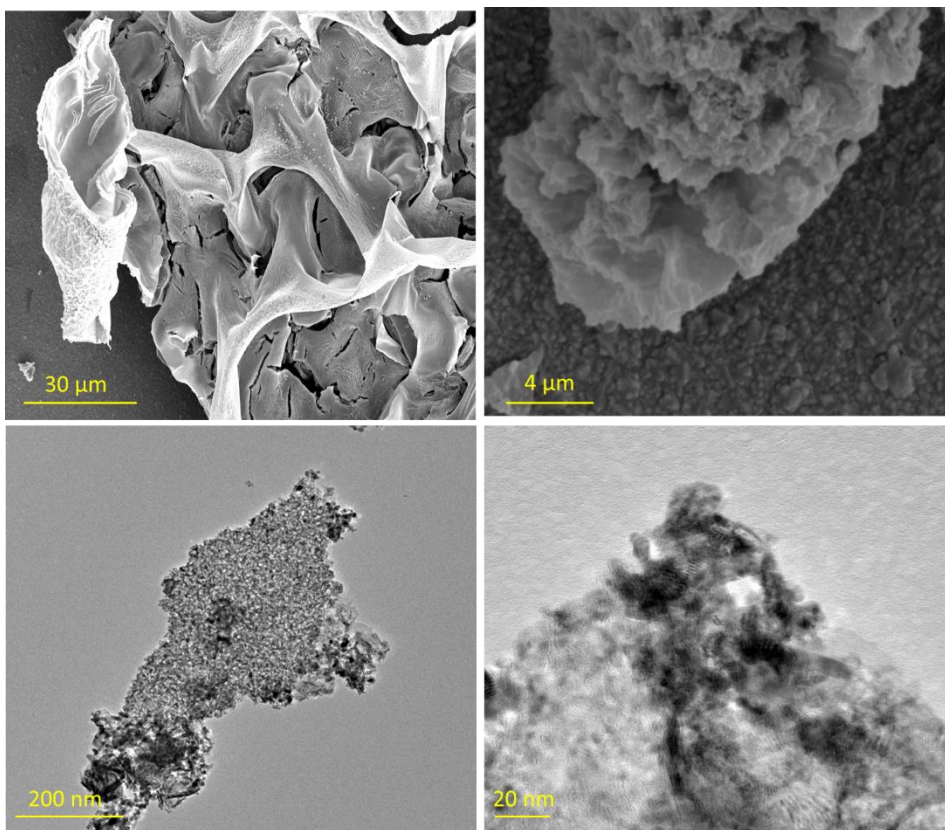


Figure S5: SEM and TEM images of Ru-Ce obtained by rapid calcination

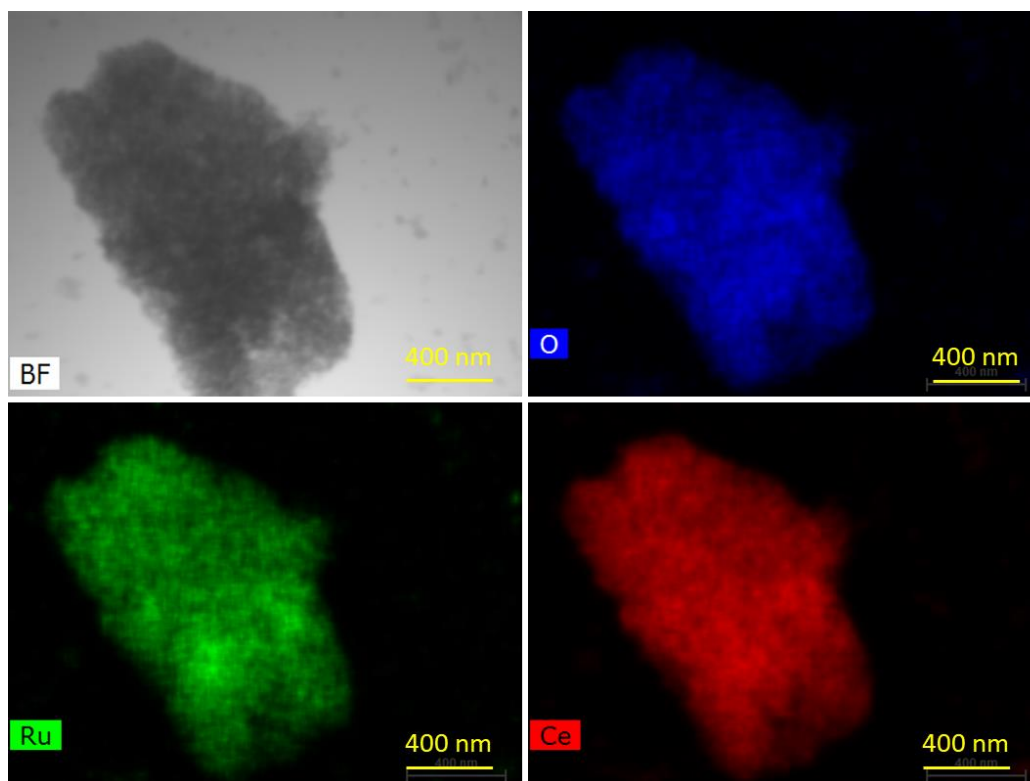


Figure S6: EDS mapping of Ru-Ce obtained by rapid calcination

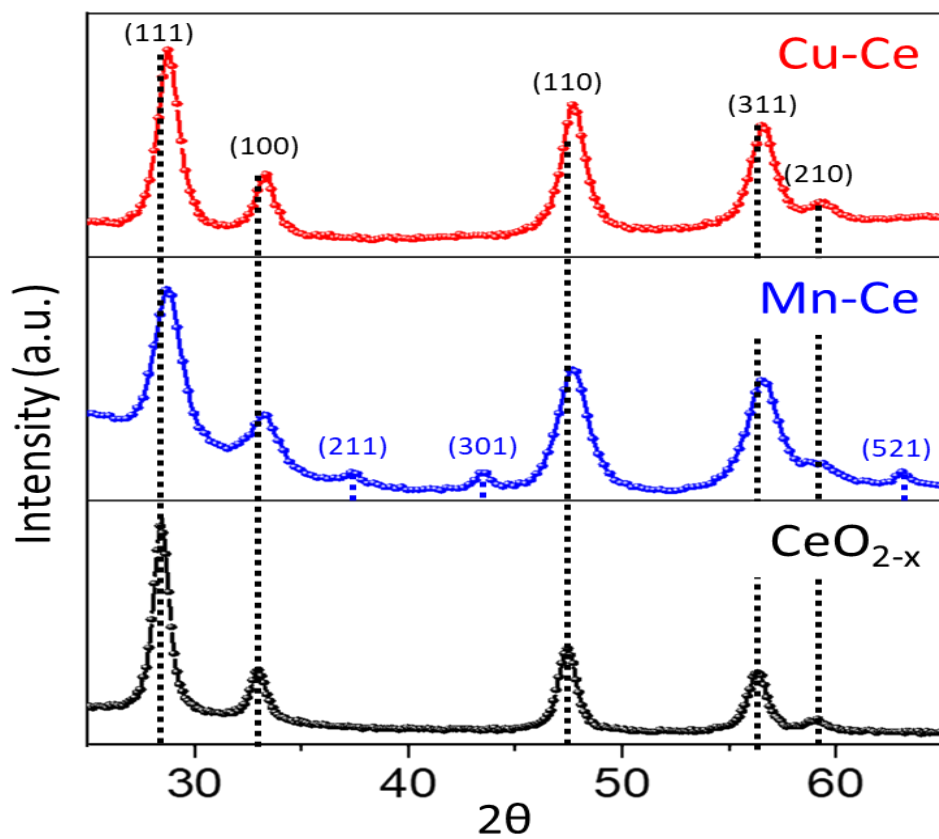


Figure S7: XRD spectra of 2D-3D CeO_{2-x} , Mn-Ce, Cu-Ce ($\alpha\text{-MnO}_2$ indicated by Miller indices in Mn-Ce)

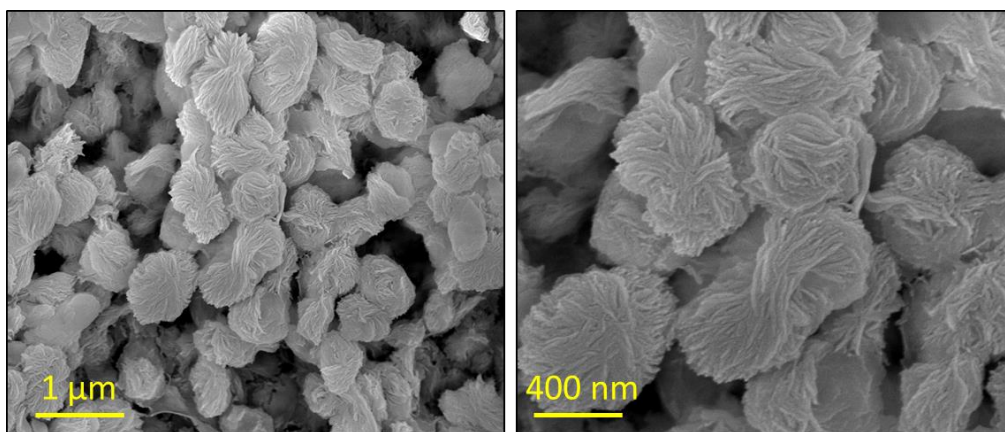


Figure S8: SEM images of Mn-Ce obtained by rapid calcination

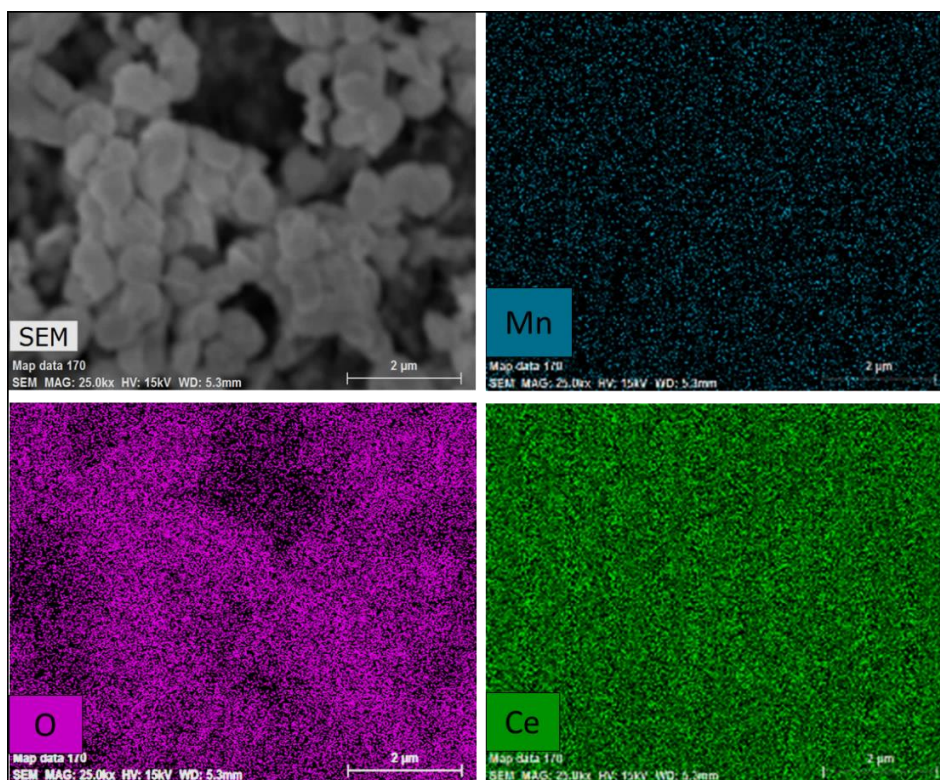


Figure S9: EDS elemental mapping of Mn-Ce obtained by rapid calcination

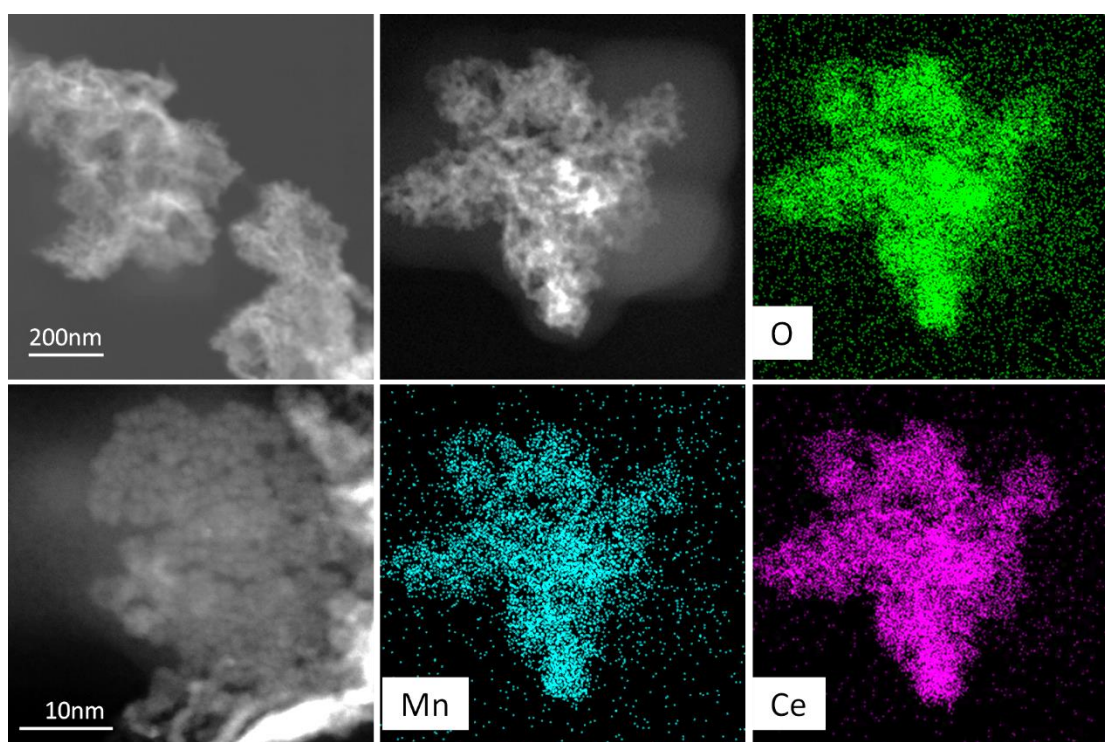


Figure S10: Dark field TEM images (left column) and STEM mapping of Mn-Ce obtained by rapid calcination (middle and right columns)

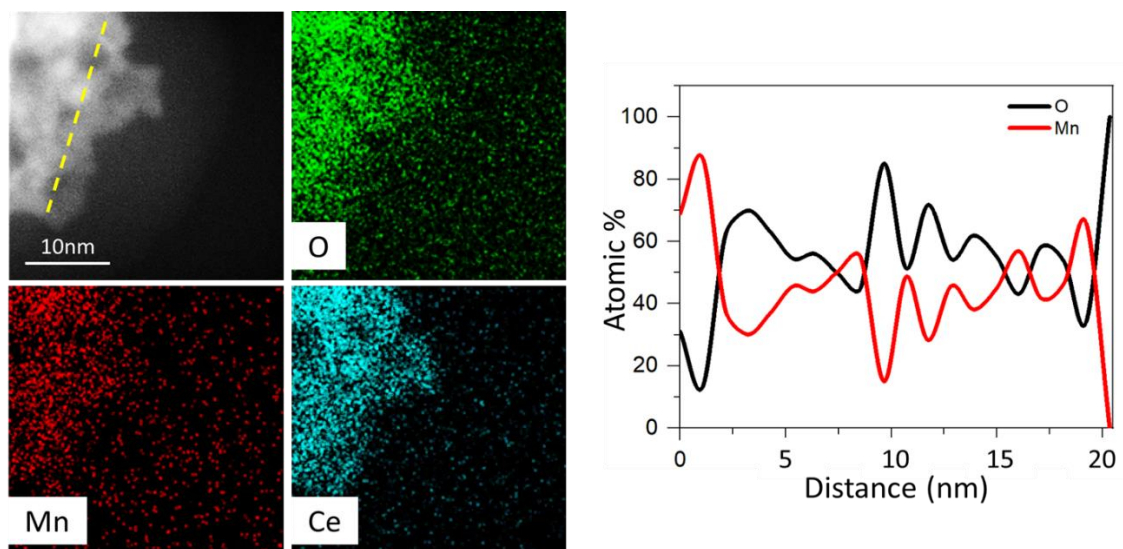


Figure S11: TEM images and STEM mapping of Mn-Ce obtained by rapid calcination

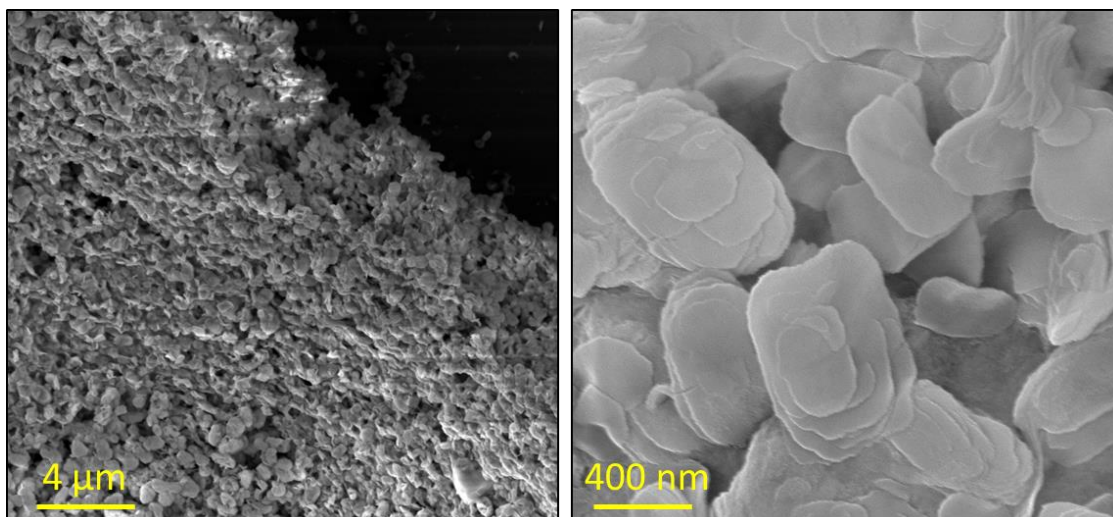


Figure S12: SEM images of Cu-Ce obtained by rapid calcination

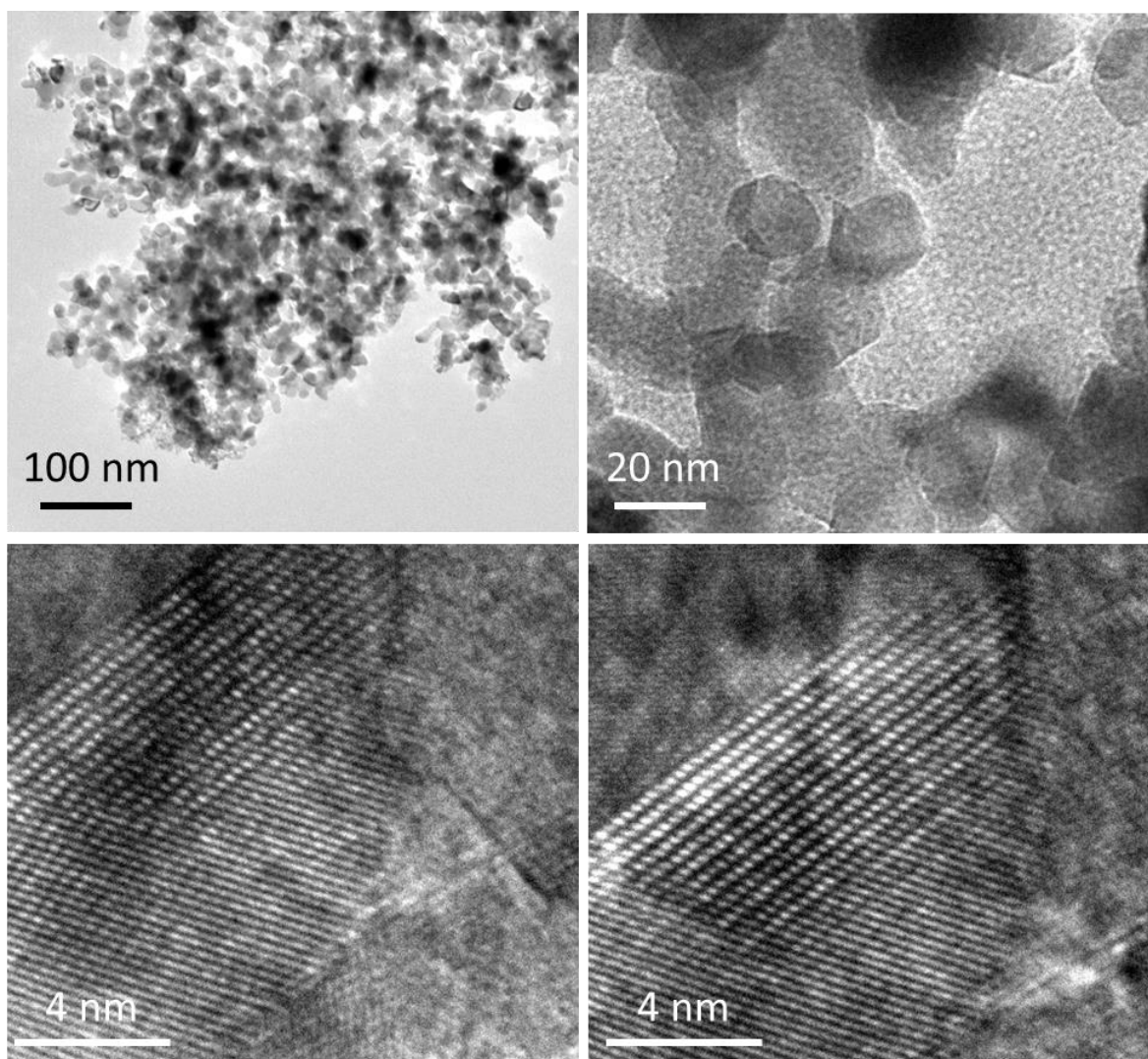


Figure S13: TEM images of Cu-Ce obtained by rapid calcination

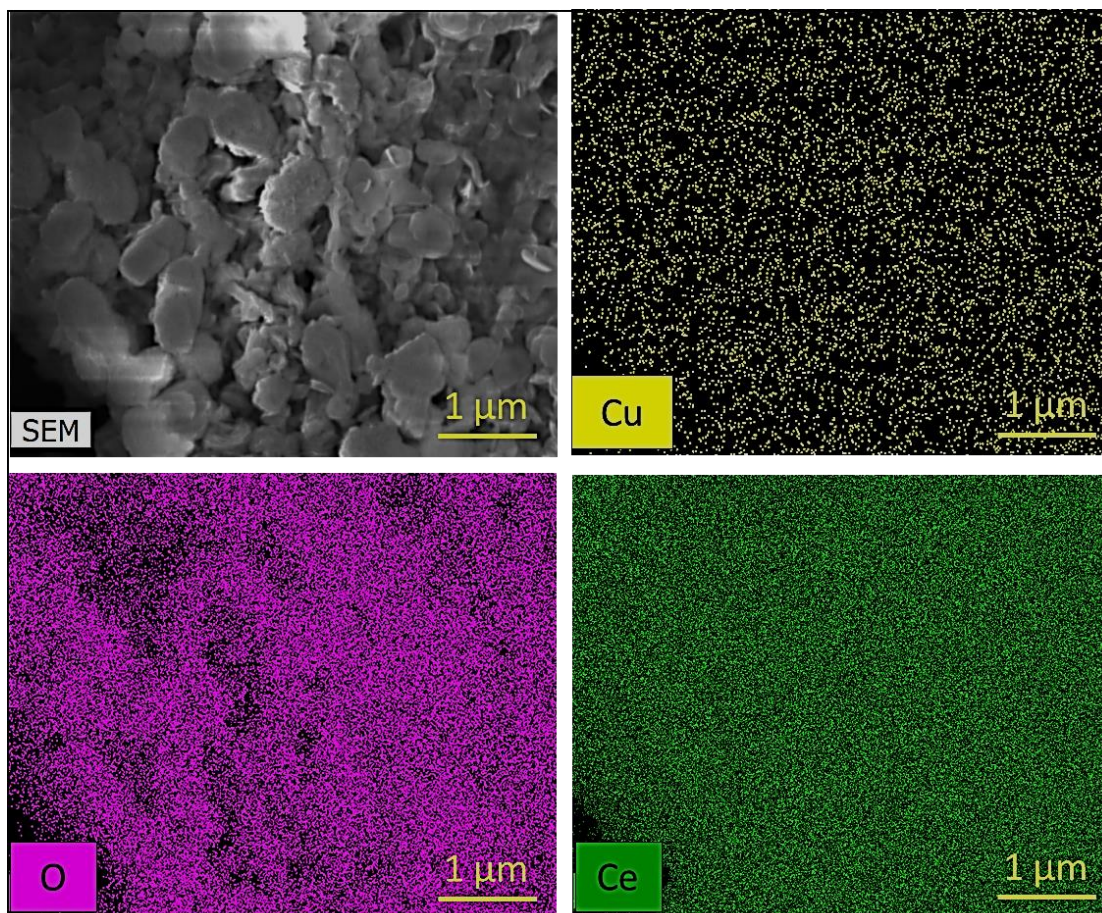


Figure S14: EDS elemental mapping of Cu-Ce obtained by rapid calcination

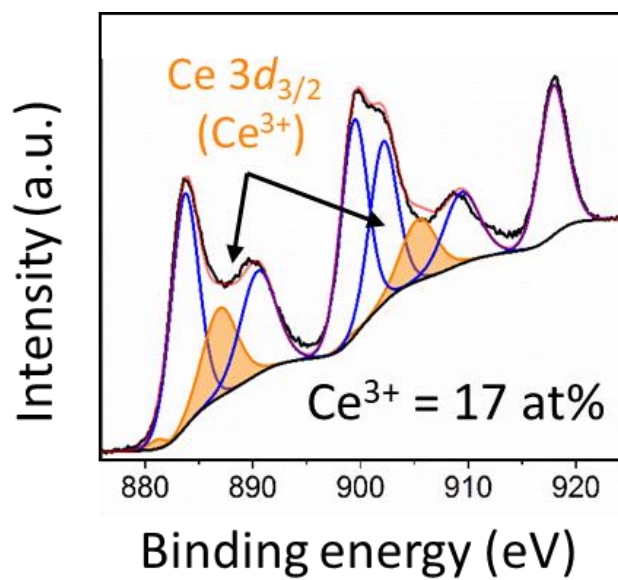


Figure S15: XPS spectra ($3d$ orbital) of Ce in 2D-3D CeO_{2-x} nanostructure

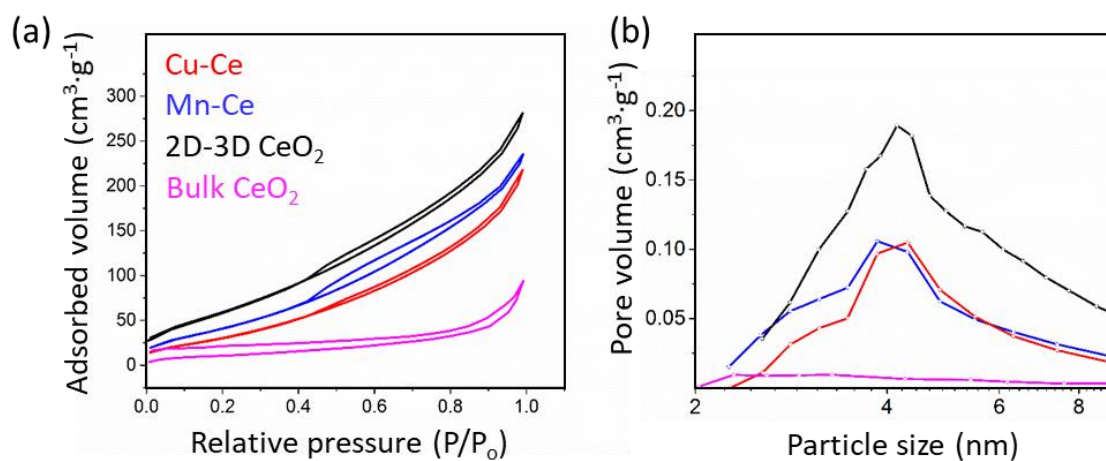


Figure S16: N₂ adsorption–desorption isotherms, (b) pore size distribution curves of CeO₂-based nanomaterials

Table S1: Specific surface areas (SSA), pore sizes, and pore volumes of CeO₂-based nanomaterials

Sample	SSA (m ² ·g ⁻¹)	Pore Size (nm)	Pore Volume (cm ³ ·g ⁻¹)
Ce-NT	51.00	3.30	0.14
2D-3D CeO _{2-x}	251.13	7.04	1.15
Cu-Ce	162.74	5.08	0.36
Mn-Ce	230.80	5.05	0.42

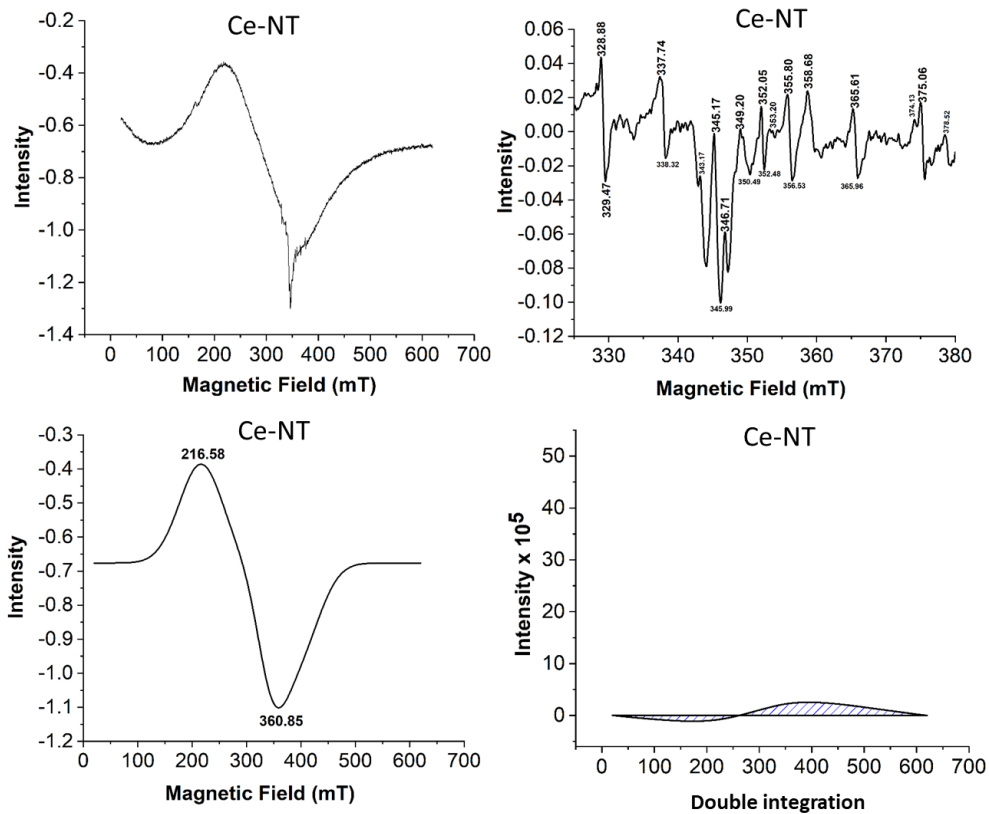


Figure S17: EPR analyses of Ce-NT

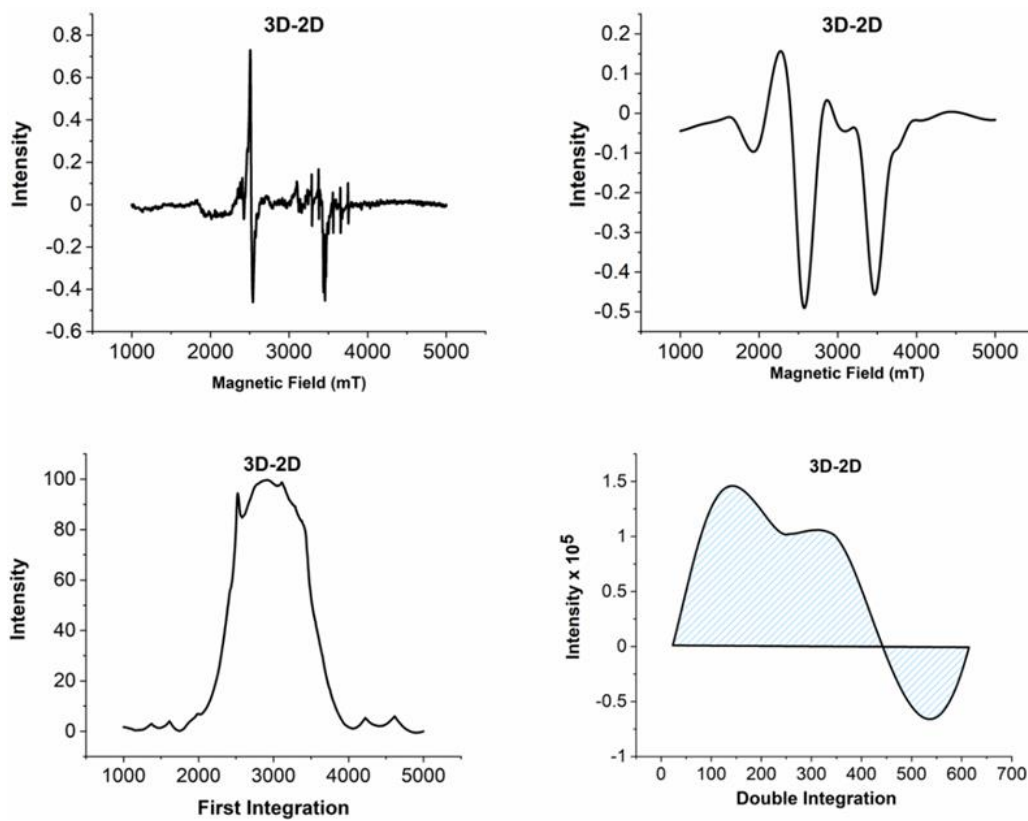


Figure S18: EPR analyses of 2D-3D CeO_{2-x}

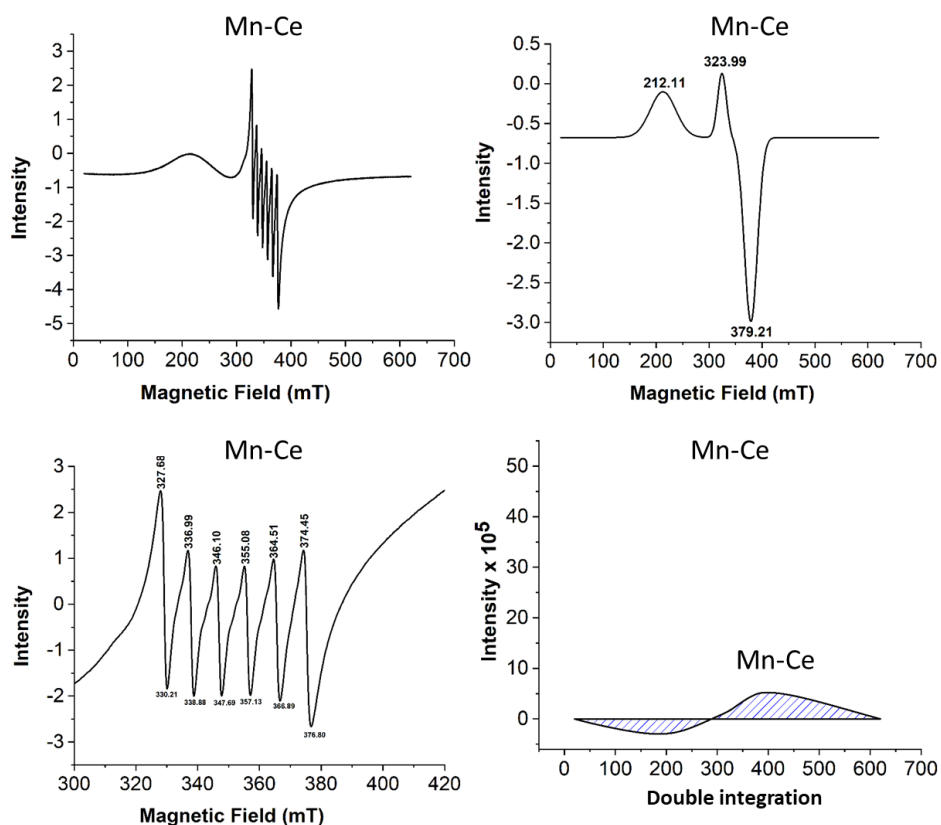


Figure S19: EPR analyses of Mn-Ce

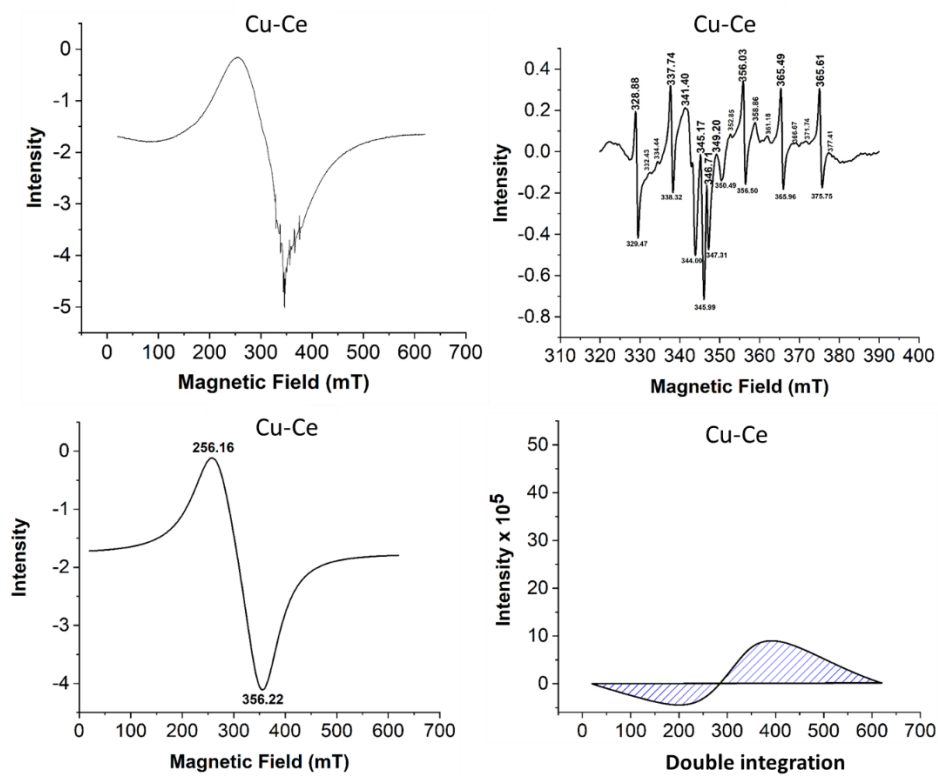


Figure S20: EPR analyses of Cu-Ce

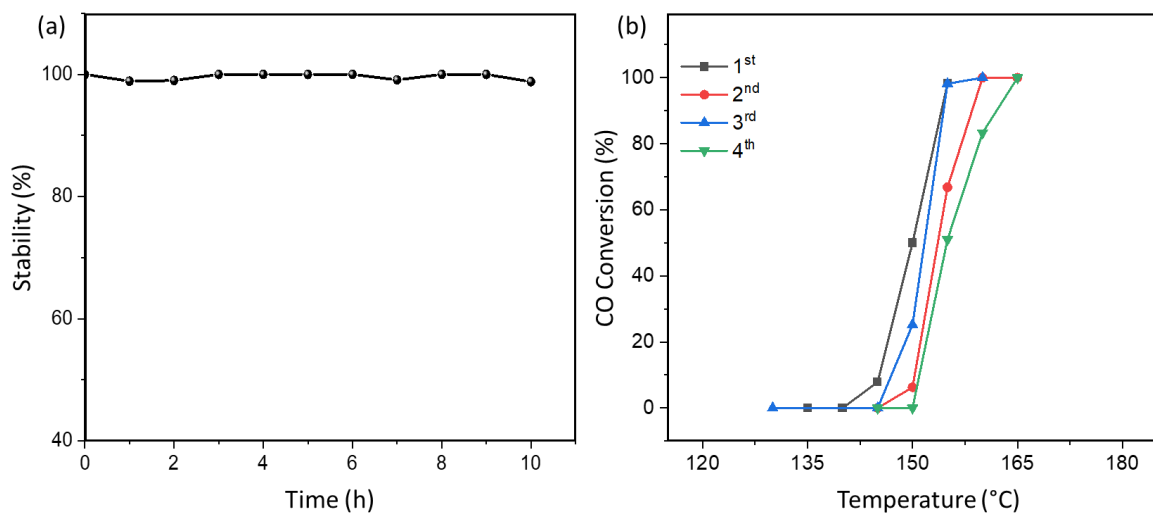


Figure S21: (a) Long-term stability test of CO oxidation reaction over 2D-3D CeO_{2-x} catalyst at a constant temperature of 165°C, (b) reusability of 2D-3D CeO_{2-x} catalyst under CO oxidation reaction conditions.

Table S2: EPR data for CeO₂-based nanomaterials

Samples	MWFQ (GHz)*	Hyperfines (mT)				g-Factors			
Ce-NT	9.861478	216.58	328.88	329.47	337.74	3.25	2.14	2.14	2.09
		338.32	343.17	345.17	345.99	2.08	2.05	2.04	2.04
		346.71	349.20	350.49	352.05	2.03	2.02	2.01	2.00
		355.80	356.53	360.85	365.61	1.98	1.98	1.95	1.93
		365.96	374.13	375.06	378.52	1.93	1.88	1.88	1.86
2D-3D CeO _{2-x}	9.856920	231.52	235.08	238.20	240.56	3.04	2.30	2.96	2.93
		247.28	250.76	258.96	264.8	2.85	2.81	2.72	2.66
		269.96	281.32	286.88	291.28	2.61	2.50	2.46	2.42
		294.72	300.76	309.96	314.12	2.39	2.34	2.27	2.24
		317.24	320.96	323.52	326.04	2.22	2.20	2.18	2.16
		328.8	337.52	341.16	343.04	2.14	2.09	2.07	2.05
		345.04	346.56	348.88	357.20	2.04	2.03	2.02	1.97
		359.64	365.2	366.8	380.28	1.96	1.93	1.92	1.85
Mn-Ce	9.861946	212.11	323.99	327.68	330.21	3.32	2.17	2.15	2.13
		336.99	338.88	346.10	347.69	2.09	2.08	2.04	2.03
		355.08	357.13	364.51	366.89	1.98	1.97	1.93	1.97
		374.45	376.80	379.21	--	1.88	1.87	1.86	--
Cu-Ce	9.861478	256.16	328.88	329.47	332.43	2.75	2.14	2.14	2.12
		334.44	337.74	338.32	341.40	2.11	2.09	2.08	2.06
		344.00	345.99	345.17	345.99	2.05	2.04	2.04	2.04
		346.71	347.31	349.20	350.49	2.03	2.03	2.02	2.01
		356.03	356.22	356.50	358.86	1.98	1.98	1.98	1.96
		361.18	365.42	365.61	365.96	1.95	1.93	1.93	1.93
		366.67	371.74	375.75	377.41	1.92	1.90	1.88	1.87

* The microwave frequencies (MWFQ) of all samples were maintained at similar values so as to allow the data (defect concentrations) to be comparable.

Table S3: Comparison of published and experimental data on catalytic CO conversion by different ceria nanostructures

Catalysts	Morphology	Dimensions (nm)	SSA (m ² ·g ⁻¹)	Pore Volume (cm ³ ·g ⁻¹)	T ₅₀	T ₁₀₀	No.	Ref.
CeO ₂	Irregular	~12	56.70	--	304	~400	1	8
CeO ₂	Nanosheet	~100	36.76	--	346	~405	2	9
CeO ₂	Nanorod	∅ 20 - 90	--	--	306	405	3	10
CeO ₂	Nanowire	∅ 8.1	76.9	--	272	~350	4	11
CeO ₂	Nanosheet	0.6	--	--	248	350	5	12
CeO ₂	Nanobundles	9.2	130.4	0.09	213	280	4	11
CeO ₂	Nanotubes	∅ ~100	-	-	250	275	6	13
CeO ₂	Irregular	8-9	55.7	--	215	260	7	14
CeO ₂	Pit-Confined Nanosheet	0.6	--	--	131	220	5	12
CeO₂	2D-3D Scaffold	4-20	251.1	1.15	144	148	Present Work	

Table S4: Comparison of published and experimental data on catalytic CO conversion by different ceria-based heterojunction nanostructures

Catalysts	Morphology	Dimensions (nm)	SSA (m ² ·g ⁻¹)	Pore Volume (cm ³ ·g ⁻¹)	T ₅₀	T ₁₀₀	No.	Ref.
CeO ₂ -Mn	Nanorod	∅ 20-90	--	--	240	275	3	10
Pd-CeO ₂	Nanocube	17	28.0	--	170	225	8	15
Cu-CeO ₂	Polyhedra	9.6	90.0	0.29	80	220	9	16
Cu-CeO ₂	Irregular	8-9	55.7	--	120	180	7	14
Pd-CeO ₂	Nanorod	∅ 11	78.0	--	127	175	8	15
Cu-CeO ₂	Nanorod	∅ 11.6	75.4	0.40	75	150	9	16
Pd-CeO ₂	Nanocube-Nanorod	∅ 9	--	--	97	>140	10	17

Au-ZrO₂-CeO₂	NP-NP-Nanosheet	10~7	--	--	55	122	11	18
CuO-CeO₂	Nanocube-NP	900-5	45.5	0.20	110	120	12	19
Au-UIO 66-CeO₂	Nanosphere	~7	870.0	0.38	72	100	13	20
Cu-CeO₂	Nanowire	∅ 20	66.4	--	75	100	14	21
Pt-CeO₂	NP-Porous Nanorod	∅ 3-9	--	--	70	80	15	22
Mn-Ce	2D-3D Scaffold	4-20	230.8	0.36	90	124	Present Work	
Cu-Ce	2D-3D Scaffold	4-20	160.0	0.42	85	88	Present Work	

References

1. C. Cazorla, B. Boronat, *Rev. Mod. Phys.*, 2017, **89**, 035003.
2. J. P. Perdew, A. Ruzsinszky, G. I. Csonka, O. A. Vydrov, G. E. Scuseria, L. A. Constantin, X. Zhou, K. Burke, *Phys. Rev. Lett.*, 2008, **100**, 136406.
3. G. Kresse, J. Furthmuller, *Phys. Rev. B*, 1996, **54**, 11169.
4. S. L. Dudarev, G. A. Botton, S. Y. Savrasov, C. J. Humphreys, A. P. Sutton, *Phys. Rev. B*, 1998, **57**, 1505.
5. P. E. Blochl, *Phys. Rev., B* 1994, **50**, 17953.
6. G. Henkelman, B. P. Uberuaga, H. A. Jonsson, *J. Chem. Phys.*, 2000, **113**, 9901-9904.
7. A. K. Sagotra, D. Chu, C. Cazorla, *Phys. Rev. Mater.*, 2019, **3**, 035405.
8. K. Kim, J. D. Yoo, S. Lee, M. Bae, J. Bae, W. Jung, J. W. Han, *ACS Appl. Mater. Inter.* **2017**, *9* (18), 15449-15458.
9. X. Zhou, J. Ling, W. Sun, Z. Shen, *J. Mater. Chem. A* **2017**, *5* (20), 9717-9722.
10. H. Du, Y. Wang, H. Arandiyana, A. Younis, J. Scott, B. Qu, T. Wan, X. Lin, J. Chen, D. Chu, *Mater. Today Commun.* **2017**, *11*, 103-111.
11. R. Rao, M. Yang, C. Li, H. Dong, S. Fang, A. Zhang, *J. Mater. Chem. A* **2015**, *3* (2), 782-788.
12. Y. Sun, Q. Liu, S. Gao, H. Cheng, F. Lei, Z. Sun, Y. Jiang, H. Su, S. Wei, Y. Xie, *Nat. Commun.* **2013**, *4*, 2899.
13. Z. Wang, J. Qi, K. Zhao, L. Zong, Z. Tang, L. Wang, R. Yu, *Mater. Chem. Front.* **2017**, *1*, 1629-1634.
14. Y. Li, Y. Cai, X. Xing, N. Chen, D. Deng, Y. Wang, *Anal. Methods.* **2015**, *7* (7), 3238-3245.
15. G. Spezzati, A. D. Benavidez, A. T. Delariva, Y. Su, J. P. Hofmann, S. Asahina, E. J. Olivier, J. H. Neethling, J. T. Miller, A. K. Datye, E. J. M. Hensen, *Appl. Catal. B-Environ.* **2019**, *243*, 36-46.
16. M. Lykaki, E. Pachatouridou, S. A. C. Carabineiro, E. Iliopoulou, C. Andriopoulou, N. Kallithrakas-Kontos, S. Boghosian, M. Konsolakis, *Appl. Catal. B-Environ* **2018**, *230*, 18-28.
17. Y. Chen, J. Chen, W. Qu, C. George, M. Aouine, P. Vernoux, X. Tang, *Chem. Commun.* **2018**, *54* (72), 10140-10143.
18. C. Du, Y. Guo, Y. Guo, X. Q. Gong, G. Lu, *J. Mater. Chem. A* **2017**, *5* (11), 5601-5611.
19. W. Li, X. Feng, Z. Zhang, X. Jin, D. Liu, Y. Zhang, *Adv. Funct. Mater.* **2018**, *28* (49), 1802559.
20. A. Yazdi, A. Abo Markeb, L. Garzón-Tovar, J. Patarroyo, J. Moral-Vico, A. Alonso, A. Sánchez, N. Bastus, I. Imaz, X. Font, V. Puentes, D. Maspoch, *J. Mater. Chem. A* **2017**, *5* (27), 13966-13970.
21. T. Kou, C. Si, J. Pinto, C. Ma, Z. Zhang, *Nanoscale* **2017**, *9* (23), 8007-8014.
22. J. Li, Y. Tang, Y. Ma, Z. Zhang,; F. F. Tao,; Y. Qu, *ACS Appl. Mater. Inter.* **2018**.